A&A, 700, A254 (2025)
https://doi.org/10.1051/0004-6361/202555597

Astronomy & Astrophysics

Measuring the initial mass of ^{44}Ti in SN 1987A through the ^{44}Sc emission line

R. Giuffrida[1,2,3,⋆], M. Miceli[1,2], E. Greco[2], S. Orlando[2], M. Ono[4,5], V. Sapienza[2], F. Bocchino[2], O. Petruk[2,6], B. Olmi[7], and S. Nagataki[8,9,10]

[1] Dipartimento di Fisica e Chimica E. Segrè, Università degli Studi di Palermo, Via Archirafi 36, 90123 Palermo, Italy
[2] INAF-Osservatorio Astronomico di Palermo, Piazza del Parlamento 1, 90134 Palermo, Italy
[3] AIM, CEA, CNRS, Université Paris-Saclay, Université de Paris, 91191 Gif sur Yvette, France
[4] Institute of Astronomy and Astrophysics, Academia Sinica, Taipei 106319, Taiwan
[5] Astrophysical Big Bang Laboratory (ABBL), RIKEN Cluster for Pioneering Research, 2-1 Hirosawa, Wako, Saitama 351-0198, Japan
[6] Institute for Applied Problems in Mechanics and Mathematics, Naukova Street 3-b, 79060 Lviv, Ukraine
[7] INAF - Osservatorio Astrofisico di Arcetri, Largo E. Fermi 5, 50125 Firenze, Italy
[8] RIKEN Center for Interdisciplinary Theoretical and Mathematical Sciences (iTHEMS), 2-1 Hirosawa, Wako, Saitama 351-0198, Japan
[9] Astrophysical Big Bang Laboratory (ABBL), RIKEN Pioneering Research Institute (PRI), 2-1 Hirosawa, Wako, Saitama 351-0198, Japan
[10] Astrophysical Big Bang Group (ABBG), Okinawa Institute of Science and Technology Graduate University (OIST), 1919-1 Tancha, Onna-son, Kunigami-gun, Okinawa 904-0495, Japan

Received 20 May 2025 / Accepted 7 July 2025

ABSTRACT

Context. Deriving the mass and large-scale asymmetries of radioactive isotopes offers valuable insights into the complex phases of a supernova explosion. Important examples include ^{56}Ni, with its decay products ^{56}Co and ^{56}Fe, and ^{44}Ti, which are studied through their X-ray emission lines, and provide a powerful diagnostic tool to probe the explosive nucleosynthesis processes in the inner layers of the exploding star.

Aims. In this framework, SN 1987A provides a privileged laboratory, being the youngest supernova remnant from which the mass of Ti has been estimated. However, some uncertainty remains in determining the initial mass of ^{44}Ti. Previous analyses, relying on *NuSTAR* and INTEGRAL data, report $M_{44} = (1.5 \pm 0.3) \times 10^{-4}\ M_{\odot}$ and $M_{44} = (3.1 \pm 0.8) \times 10^{-4} M_{\odot}$, respectively. In this paper, we estimate the initial mass of ^{44}Ti via its decay product, the ^{44}Sc emission line at 4.09 keV, using *Chandra* observations.

Methods. We performed multi-epoch spectral analysis focusing on the inner part of the remnant, to minimize the contamination from the X-ray emission stemming from the shocked plasma. As a result, we report the detection of ^{44}Sc emission line in the central part of SN 1987A with a ∼99.7% (3 σ) significance.

Results. The simultaneous fit of the spectra extracted from observations between 2016 and 2021 yields a line flux of $6.8^{+2.2}_{-2.3} \times 10^{-7}$ photons s^{-1} cm^{-2}, corresponding to a ^{44}Ti mass of $M_{44} = (1.6 \pm 0.5) \times 10^{-4} M_{\odot}$ (errors at the 90% confidence level). The results obtained with our spectral analysis appear to align with those derived with *NuSTAR*.

Key words. supernovae: general – ISM: general – supernovae: individual: SN 1987A

1. Introduction

Supernova (SN) explosions are important sources for studying the chemical evolution of the Universe. The supernova ejecta carry information on explosive nucleosynthesis processes, and elements synthesized in the inner layers of core-collapse supernovae can "retain memory" of the physical mechanisms governing the explosion. Several key issues can be addressed by studying the radioactive emission of the ^{56}Ni and ^{44}Ti isotopes, which are synthesized in the central part of the exploding star (Hashimoto 1995; Nagataki et al. 1997; Nagataki 2000), along with their daughter products, such as ^{56}Co and ^{56}Fe for ^{56}Ni, and ^{44}Sc for ^{44}Ti. In particular, the yield of ^{44}Ti is very sensitive to supernova shock conditions (more so than ^{56}Ni), specifically the peak temperature and density of the ejecta reached shortly after core collapse (e.g., Magkotsios et al. 2010), thus providing a powerful diagnostic tool for explosion physics. Moreover, as shown by Nagataki et al. 1997, 1998 and Nagataki (2000), a high ^{44}Ti/^{56}Ni ratio can be considered a signature of large-scale anisotropies in the explosions. More recently it has been found that neutrino-driven winds and the possible simultaneous accretion and explosion in 3D models of CCSNe are crucial for ^{44}Ti production (Wang & Burrows 2024).

After the complete decay of ^{56}Co and ^{57}Co, which dominate the energy balance during the first few years following the explosion, the IR, optical, and UV emissions are driven by the radioactive decay of ^{44}Ti. Additional evidence for the presence of ^{44}Ti can be derived from the X-ray and γ-ray emission of its decay chain. In this process, ^{44}Ti decays into ^{44}Sc with an e-folding time of 85 years (Ahmad et al. 2006), producing two emission lines at 67.9 keV and 78.4 keV through electron capture. Subsequently, ^{44}Sc decays into ^{44}Ca with a lifetime of

⋆ Corresponding author.

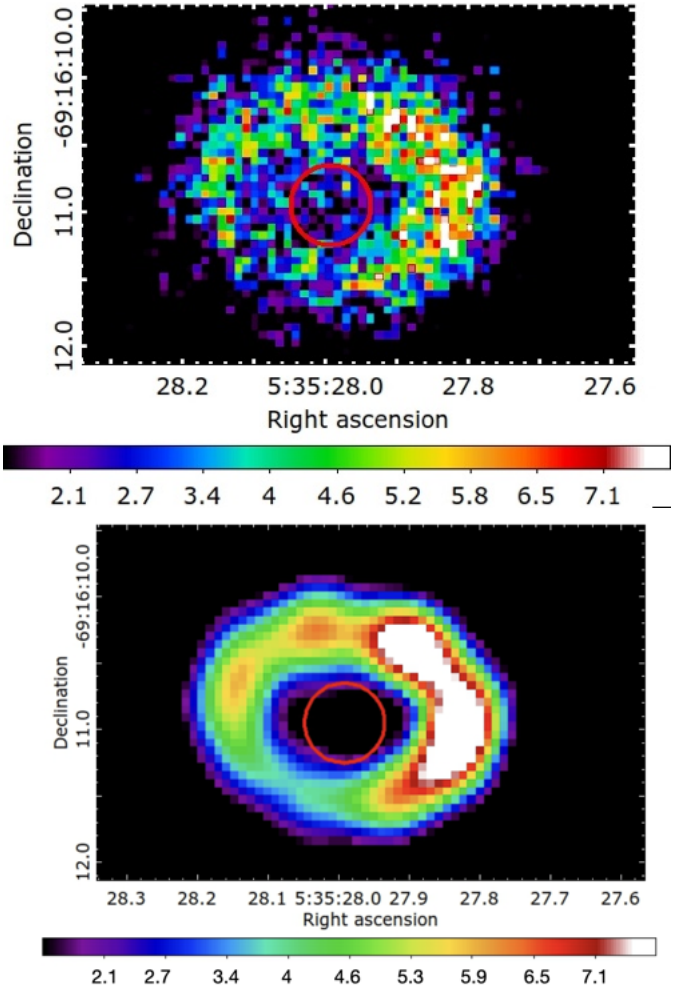

Fig. 1. *Upper panel*: *Chandra*/ACIS photon count map of SN 1987A in 2019 (Obs ID 21304), in the 0.5–7.0 keV energy band. *Lower panel*: same image as above, but deconvolved using the Lucy-Richardson algorithm. Both images have a pixel size of 0.06″. The red circle indicates the region selected for spectral analysis.

5.7 hours (Ahmad et al. 2006), emitting a line at 1157.0 keV through β-decay and electron capture. The electron capture results in ^{44}Sc with a vacancy in its K-shell, which produces a K-shell transition with an X-ray emission line at 4.09 keV.

The supernova SN 1987A, observed on February 23, 1987 in the Large Magellanic Cloud (West 1987) at a distance d = 51.4 kpc (Panagia 1999), is an ideal target for studying a nearby, very young, core-collapse supernova explosion (CCSN), and its subsequent evolution into a supernova remnant (SNR). X-ray emission from SN 1987A was detected by Dotani et al. (1987) in the hard band (above 10 keV) a few months after the explosion and a few years later by Beuermann et al. (1994) with *ROSAT* in the soft X-rays. Since 1999, multi-epoch *Chandra* observations have revealed the morphology of the X-ray emission and its time evolution (Helder et al. 2013; Frank et al. 2016; Ravi et al. 2024; see also Fig. 1). The X-ray emission of SN 1987A is characterized by a ring-like structure in expansion, which results from the shocked circumstellar medium produced by stellar winds from the progenitor star before the SN explosion. The circumstellar medium has been previously observed in the optical band (Luo & McCray 1991; Lundqvist & Fransson 1991; Burrows et al. 1995; Chevalier & Dwarkadas 1995). Important information on the origin and evolution of the X-ray spectral features has been obtained from the analysis of *XMM-Newton* observations (Haberl et al. 2006; Sun et al. 2021) and SRG/eRosita (Maitra et al. 2022).

The X-ray emission can be well reproduced by magneto-hydrodynamic (MHD) simulations (Orlando et al. 2015, 2019, 2020, 2025), which self-consistently describe the time evolution of the remnant morphology, fluxes, and spectra. Moreover, the comparison between X-ray data and MHD simulations provides important information on the origin of the broadening of X-ray emission lines, pinpointing the roles of thermal broadening and Doppler broadening associated with plasma expansion (Miceli et al. 2019; Ravi et al. 2021; Miceli 2023). Recently, XRISM collaboration (2025) have shown that *XRISM* observations can recover the expansion velocity of the outer (i.e., metal-poor) ejecta layers interacting with the reverse shock, as predicted by Sapienza et al. (2024a,b). Thermal X-ray emission from metal-rich ejecta is expected to be modest in the next few years (Orlando et al. 2025).

Multiwavelength observations of SN 1987A have revealed Doppler shifts in the emission lines of heavy elements (e.g., [Fe II] and [Ni II]) up to velocities exceeding 3000 km s^{-1} (e.g., Haas et al. 1990; Colgan et al. 1994; Utrobin et al. 1995; Larsson et al. 2016). The formation of ^{56}Co gamma-ray lines in SN 1987A, several months earlier than expected (Matz et al. 1988), reveals mixing between some innermost heavy nuclear products and the outer envelope. The ^{56}Co lines at 847 and 1238 keV were detected by balloon experiments (Cook et al. 1988; Mahoney et al. 1988; Sandie et al. 1988; Teegarden et al. 1989) and by the γ-ray spectrometer (GRS) on board the Solar Maximum Mission (SMM) satellite (Matz et al. 1988; Leising & Share 1990). As a result, it was found that almost 5% of iron-group-rich plasma mixed out to velocities of ∼3000 km s^{-1} (Arnett et al. 1989; Leising & Share 1990), much higher than the characteristic values ($\lesssim$ 1000 km s^{-1}) expected for iron-group material. This mixing may result from Rayleigh–Taylor instabilities or from radioactive heating, which causes the expansion of ^{56}Ni/^{56}Co-rich bubbles (Basko 1994; Kifonidis et al. 2003; Urushibata et al. 2018; Ono et al. 2020).

The anisotropy in the inner ejecta velocities has been confirmed by the detection of a redshift of approximately 0.23 keV in the ^{44}Ti X-ray emission lines at 67.87 keV (Boggs et al. 2015), observed with *NuSTAR* and corresponding to a velocity of ∼700 km s^{-1} in the rest frame of SN 1987A. Boggs et al. (2015) measured the flux of the line at 67.87 keV (F_{68} = $3.5 \pm 0.7 \times 10^{-6}$ cm^{-2} s^{-1}; similar results were later obtained by Alp et al. 2021), thus deriving an initial mass of ^{44}Ti M_{44} = $1.5 \pm 0.3 \times 10^{-4} M_{\odot}$ (see Eq. (1)). This value is in agreement with the simulations (Thielemann et al. 1990; Woosley & Hoffman 1991), which predict M_{44} = 0.2–2.5 $\times 10^{-4} M_{\odot}$ in CCSNe. Modeling of the optical spectrum performed by Jerkstrand et al. (2011) also suggests $M_{44} = 1.5 \pm 0.5 \times 10^{-4} M_{\odot}$. Furthermore, model B18.3 developed by Orlando et al. (2020) and Ono et al. (2020) predicted an initial ^{44}Ti mass of approximately $1.4 \times 10^{-4} M_{\odot}$. However, this value should be interpreted with caution, as the explosive nucleosynthesis was modeled using a small approximate nuclear reaction network and this may lead to an overestimation of the ^{44}Ti abundance (Mao et al. 2015).

Conversely, the fluxes of the 67.87 keV and 78.32 keV lines measured with INTEGRAL indicate a higher initial ^{44}Ti mass, by a factor of ∼2, i.e., $M_{44} = (3.1 \pm 0.8) \times 10^{-4}\ M_{\odot}$ (Grebenev et al. 2012).

The ^{44}Ti yield can also be estimated by measuring the flux of the ^{44}Sc line at 4.09 keV, as successfully demonstrated for

the supernova remnant G1.9+0.3 by Borkowski et al. (2010), through the analysis of *Chandra* observations. This approach was also applied to SN 1987A by Leising (2006), who analyzed multi-epoch *Chandra* spectra of the entire remnant, finding no significant detection of the ^{44}Sc line due to high contamination by the emission of the shocked ring material. Their upper limit on the line flux corresponds to $M_{44} < 2 \times 10^{-4}\ M_{\odot}$, without including the effects of photoelectric absorption from the surrounding cold ejecta.

In this paper, we adopt a new methodology to detect the ^{44}Sc line in multi-epoch *Chandra* observations of SN 1987A and to estimate the value of M_{44}. In particular, we selected a circular region in the inner part of the remnant (with an angular radius $R \sim 0.3''$; see Fig. 1), where the contamination from thermal emission from the shocked plasma is as low as possible. Additionally, the expansion of the bright ring reduces contamination from thermal emission from shocked plasma in the central region, where ^{44}Sc is thought to be synthesized, at the latest epochs. We also note that the lowest absorption from the cold ejecta at the latest epochs favors the detection of the ^{44}Sc emission line.

The paper is organized as follows. Sect. 2 describes the observations analyzed and the data reduction. Results are presented in Sects. 3 and 4 and the discussion and conclusions are provided in Sect. 5. Details of the observations are listed in Appendix A. Appendix B shows the temporal evolution of the ^{44}Sc line. The background region and spectrum are presented in Appendix C, while Appendix D shows the complete view of the Markov Chain Monte Carlo (MCMC) corner plot discussed in Sect. 3.

2. Observations and data reduction

We analyzed all archival *Chandra*/ACIS-S observations of SN 1987A, spanning 22 years from 2000 to 2021. The relevant information on the observations is summarized in Table A.1. Data were analyzed with *CIAO* (v4.13), using *CALDB* (v4.9.4), and reprocessed with the *chandra_repro* task.

For the image analysis, we adopted subpixel sampling with a pixel size of 0.06 arcsec for each observation. We improved the spatial resolution of all images using the *CIAO* `arestore` tool, which accounts for the point spread function (PSF) of the telescope by applying the Lucy-Richardson deconvolution algorithm (as previously demonstrated in Helder et al. 2013; Frank et al. 2016; Ravi et al. 2024). To produce the PSF for the deconvolution, we used the `MARX` software (Davis et al. 2012). The deconvolved image provides a better constraint on the emission from the ring, serving as a good starting point for selecting the region used in the spectral analysis.

Spectra were extracted from the event files using *specextract*, which also generates the corresponding ancillary response file (ARF) and the redistribution matrix file (RMF). The spectra were rebinned using the optimal binning algorithm of (Kaastra & Bleeker 2016). Spectra extracted from observations performed within one month were merged using the *CIAO* tool `combine_spectra`.

Spectra were analyzed using the *XSPEC* V 12.13.0c software(Arnaud 1996), in the 1.0–5.5 keV band. Due to the low statistics, we fit the spectra using the C-statistic (Cash 1979). To calculate the error bars, we ran the Markov Chain Monte Carlo (MCMC) algorithm within `xspec`, thereby accounting for the dependencies among the free parameters in the fit. We used the Goodman–Weare algorithm with a chain length of 2×10^5 and 30 walkers.

3. Results

The isotope ^{44}Ti is synthesized in the innermost ejecta, and its X-ray emission becomes detectable only when the gas is optically thin, i.e., approximately 20 years after the SN explosion (e.g., Fransson & Chevalier 1987). Once the ejecta become transparent to X-rays, the flux corresponding to each radioactive emission line, F_i, can be calculated as

$$F_i = \frac{M_{44} W_i}{4\pi d^2 44 m_p t_{44}} e^{-t/t_{44}}, \quad (1)$$

where M_{44} is the initial mass of ^{44}Ti, d is the distance to the source, m_p is the proton mass, t_{44} is the e-folding time decay of ^{44}Ti (~85 yr), and W_i is the emission efficiency for the three X-ray emission lines (17.4% for line at 4.1 keV, 87.7% for line at 67.87 keV, and 94.7% for line at 78.4 keV, Grebenev et al. 2012).

We expect ^{44}Ti in SN 1987A to be distributed over an extended area, similar to that of Fe-rich ejecta. Larsson et al. (2023) showed that the Fe-rich ejecta are located within the main shell of reverse-shocked material, in a region referred to as the homunculus, well inside the shocked, dense equatorial ring (ER). Accordingly, we selected a circular region with radius $0.3''$ (shown as a red circle in Fig. 1) for spectral extraction. Within this region, maximum ^{44}Sc line emission is expected from the unshocked ejecta, while, the choice of extraction region simultaneously minimizes the contamination associated with the thermal X-ray emission from the ER.

The source spectrum was fitted with a model that includes interstellar absorption (the `Tbabs` model) with a column density, N_H, fixed at 2.35×10^{21} cm^{-2} (Park et al. 2006); a non-equilibrium of ionization collisional plasma model (the`vnei` model), to reproduce thermal emission from the shocked plasma spilling from the bright ring inside the central region because of the telescope PSF; an absorbed power law (with absorption originating from cold ejecta) to account for the nonthermal emission stemming from the putative pulsar wind nebula (Greco et al. 2021, 2022) (the `vphabs*pow` model); and a Gaussian component for the ^{44}Sc line. The ^{44}Sc line emission is expected to be redshifted as that of ^{44}Ti ($(\Delta E/E)_{^{44}\mathrm{Ti}} = (\Delta E/E)_{^{44}\mathrm{Sc}}$). Since the emission line at 67.87 keV shows $(\Delta E)_{^{44}\mathrm{Ti}} = 0.23 \pm 0.09$ (Boggs et al. 2015), we expect $(\Delta E)_{^{44}Sc} = 0.013 \pm 0.005$ keV, yielding the line centered at about 4.076 keV. We kept the line centroid frozen to this value during the fitting process. The model for the source spectra is described by the following equation:

$$Src\ mod = Tbabs \times (vphabs \times pow + vnei + gauss) \quad (2)$$

In the early *Chandra* observations, we expect the absorption from cold ejecta to be prominent at the energy of the ^{44}Sc emission line and the measurement of the line flux to be affected by this issue. A careful search for line emission at 4.076 keV yields very low line fluxes for the observations performed between 2000 and 2015, as described in detail in Appendix B. The detailed modeling of the time-dependent absorption from cold ejecta is beyond the scope of this paper. Given the uncertainties in the distribution of ^{44}Ti in our simulations of SN 1987A (see Ono et al. 2020), it is not possible to perform an accurate estimate of the emission and absorption of the line in the ejecta. However, we caution that this limitation may affect our estimates. We focus here on the spectral analysis of the most recent six years of our set of observations (2016–2021), when the expansion of the remnant significantly reduces thermal contamination in the central region, and the cold ejecta are expected to be optically thin, thereby allowing Eq. (1) to be applied.

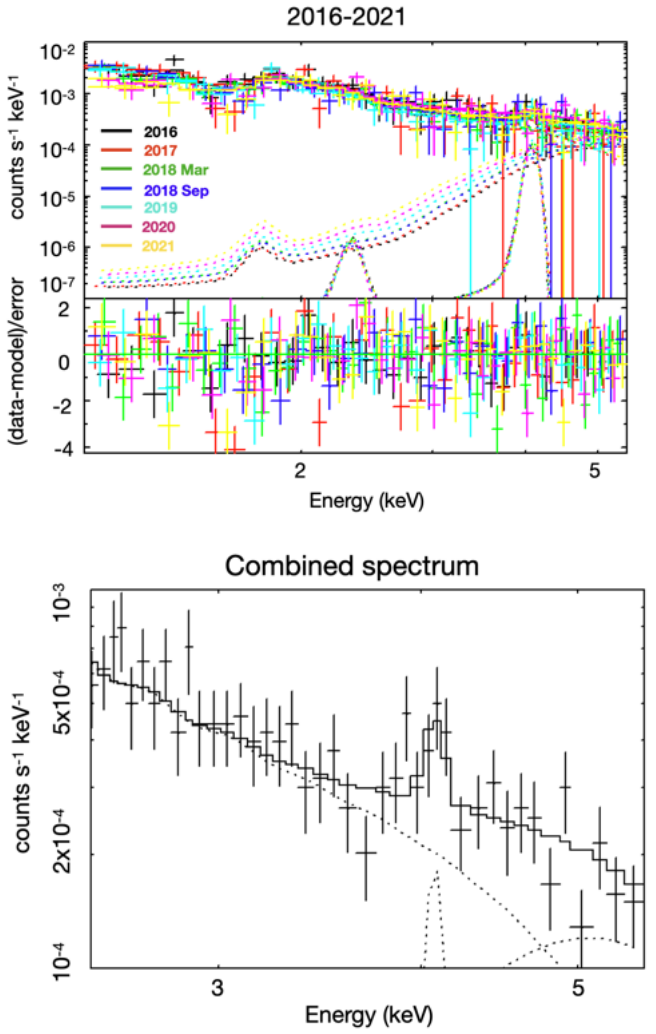

Fig. 2. *Upper panel*: *Chandra*/ACIS spectra extracted from the circular region shown in Fig. 1 for all observations performed between 2016 and 2021 (see Table A.1), with the corresponding best-fit model and residuals. Dotted lines show each component of the best fit model for each epochs. *Lower panel*: combined spectrum obtained by summing all the observations shown in the upper panel. The ^{44}Sc line is modelled by a narrow Gaussian at 4.076 keV. Dotted lines indicate the different components of the best-fit model.

To improve the statistics of the ^{44}Sc emission line, we simultaneously fit spectra extracted from all observations performed between 2016 and 2021. When fitting the spectra, the electron temperature, ionization parameter, and normalization of the `vnei` component of each spectrum were left free to vary. The normalization of the Gaussian component that models the ^{44} Sc line was also a free parameter, but, in this case, the normalizations of different epochs were tied together to account for the expected exponential time decay of Eq. (1). The sigma of the Gaussian component was fixed to 1×10^{-3} keV to reduce the number of free parameters. We verified that the results of the fits were not affected when this parameter was left free to vary.

The background region was selected on the same chip as the source region, in an area without visible point-like sources, and the corresponding spectrum was fitted with an ad hoc model (see Appendix C for details). The background flux is consistently less than 0.1% of the total, which is why the background components are not visible in the spectral plots. The data, corresponding best-fit model, and residuals are shown in the upper panel of Fig. 2.

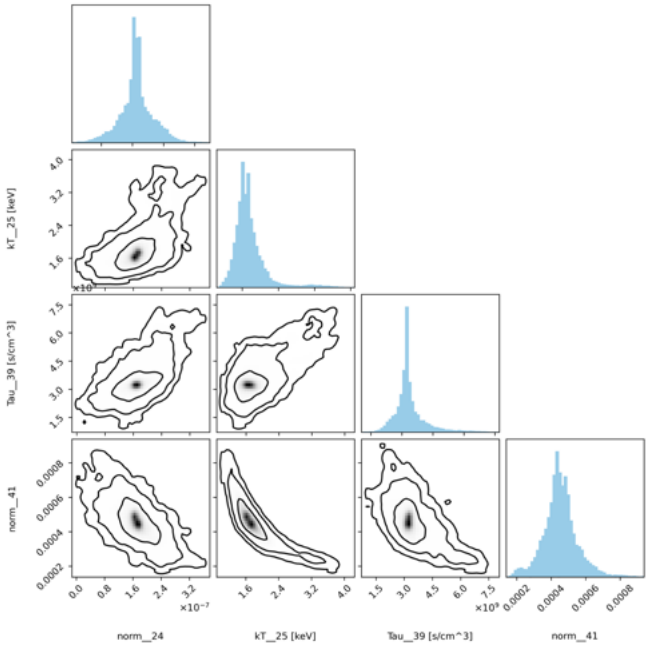

Fig. 3. Close-up view of the MCMC corner plot shown in Fig. D.1. The parameter `norm_24` indicates the normalization of the Gaussian at 4.076 keV, not corrected for the PSF effects (see text). The parameters `kT_25, Tau_39, and norm_41` correspond to the temperature, ionization parameter, and normalization, respectively, for the `vnei` component in the 2016 spectrum.

The angular extension of the spectral extraction region shown in Fig. 1 (0.3″) is smaller than the *Chandra* PSF (~0.5″), so that a fraction of the photons emitted within the central region are scattered outside it by the telescope mirrors. Larsson et al. (2023) showed that the unshocked Fe-rich ejecta in SN 1987A extend over a large area inside the ER, largely filling the spectral extraction region. As a working assumption, we assume that the Ti-rich ejecta are uniformly distributed within the extraction region (Ono et al. 2020). Under this hypothesis, the ^{44}Sc line emission originates from a disk with radius 0.3″. Using the `MARX` software, we find that, in this scenario, three-quarters of the photons are scattered outside the region. A very similar proportion (71%) is obtained by assuming a 2D Gaussian profile with $\sigma = 0.15''$. Although this percentage may vary slightly depending on different spatial distributions of surface brightness within the extraction region, we expect that the line flux obtained from the spectral analysis needs to be multiplied by a factor f of the order of $f \approx 4$ to recover its intrinsic value. We adopt $f = 4$ hereafter.

From the combined analysis of the 2016–2021 spectra, we find a line flux of $6.8^{+2.2}_{-2.3} \times 10^{-7}$ photons s^{-1} cm^{-2}, with error bars at the 90% confidence level. For visualization purposes, the lower panel of Fig. 2 shows the combined *Chandra*/ACIS spectrum obtained by summing all spectra collected between 2016 and 2021. The ^{44}Sc line is clearly visible above the continuum. Fig. 3 shows a portion of the MCMC corner plot for the first four free parameters: the normalization of the Gaussian centered at 4.076, the electron temperature kT, the ionization age τ, and the normalization of the first `vnei` component associated with the spectrum observed in 2016. Contours correspond to the 68%, 95.5%, and 99.7% confidence levels. The corresponding complete corner plot is shown in Fig. D.1 and indicates a detection significance of approximately 3σ (99.7% confidence level). We

conclude that the detection of the line is robust and statistically significant.

Using Eq. (1) and setting W_i to 0.174 (see Sect. 1), we can estimate the initial mass of ^{44}Ti from the ^{44}Sc line flux reported above, finding $M_{44} = 1.6 \pm 0.5 \times 10^{-4}$ M$_\odot$, with error bars at the 90% confidence level. This result is in excellent agreement with the value obtained from the analysis of *NuSTAR* spectra by Boggs et al. (2015). However, our estimate of the ^{44}Ti initial mass is significantly lower than that reported by Grebenev et al. (2012), based on the analysis of INTEGRAL data.

4. XRISM-Resolve simulated spectra

The detection of the ^{44}Sc line might be feasible with the new X-ray telescope, XRISM. SN 1987A will not be spatially resolved by the XRISM mirrors; therefore, it will not be possible to extract spectra from small regions to reduce contamination from thermal X-ray emission, as was done with *Chandra*. However, the high spectral resolution offered by the XRISM-Resolve spectrometer will facilitate detection of the line emerge over the continuum.

We simulated XRISM-Resolve spectra for the year 2025 using a phenomenological model that reproduces the spectrum from Sapienza et al. (2024a,b), including the effects of the gate valve closing. We assumed an exposure time of 400 ks, which is similar to the actual exposure time for SN 1987A in the XRSIM Performance Verification Phase observation. We added a Gaussian component to this model to account for the ^{44}Sc line, along with an absorbed power law (Greco et al. 2021, 2022) for the year 2024 to account for the emission of the putative Pulsar Wind Nebula (PWN). Figure 4 shows the simulated spectra obtained by assuming two different ^{44}Sc line widths (the line being Doppler-broadened because of the rapid expansion of the ejecta), namely 1000 km s^{-1} and 2000 km s^{-1}, in the left and right panels, respectively.

The detectability of the line strongly depends on its broadening. For an expansion velocity of 1000 km s^{-1}, the significance of the detection exceeds the 99% confidence level. However, assuming a much more reasonable value of 2000 km s^{-1} for the expansion velocity, the analysis of the synthetic spectrum shows a non-detection of the ^{44}Sc line, with its flux being larger than zero at only the 68% confidence level. These results therefore indicate a non-detection of the ^{44}Sc line with XRISM-Resolve, in agreement with the recent findings of XRISM collaboration (2025).

5. Discussion and conclusion

The study of ^{44}Ti in SNRs plays a crucial role in understanding the physical processes governing the explosion of massive stars. Previous studies have detected radioactive emission lines of ^{44}Ti in SN 1987A (Boggs et al. 2015; Grebenev et al. 2012), although *NuSTAR* and INTEGRAL spectra yield different fluxes, leaving the initial mass of ^{44}Ti still under debate. In particular, using the relation between the flux and the initial mass of ^{44}Ti, Eq. (1), a value of $M_{44} = (1.5 \pm 0.3) \times 10^{-4} M_\odot$ was derived from *NuSTAR* data (Boggs et al. 2015), while $M_{44} = (3.1 \pm 0.8) \times 10^{-4} M_\odot$ was obtained from INTEGRAL (Grebenev et al. 2012). Another method of measuring the initial mass of ^{44}Ti involves the emission line of ^{44}Sc, which is a product of the ^{44} Ti decay chain.

In this work, we performed a systematic search for the ^{44}Sc line by analyzing multi-epoch *Chandra* observations of SN 1987A (from 2000 to 2021). We exploited the remarkable spatial resolution of the *Chandra* mirrors to extract X-ray spectra from a small region (radius 0.3 arcsec) in the center of the remnant, as shown in Fig. 1.

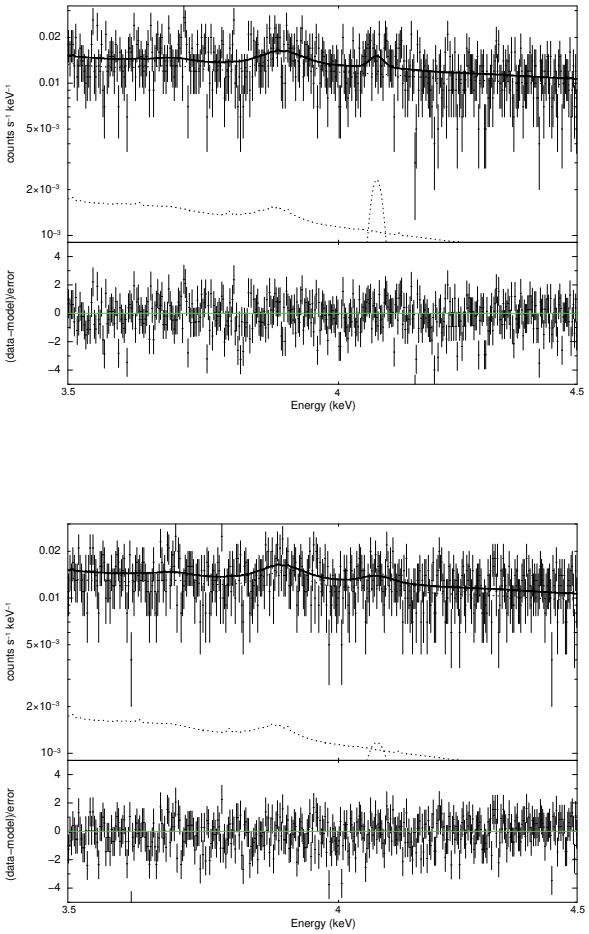

Fig. 4. Synthetic XRISM-Resolve spectra produced using the model by Sapienza et al. (2024a) with the addition of the expected Scandium line for the year 2025, and with updated RMF and ARF including the effects of the closed gate valve (Sapienza et al. 2024b). Dotted lines show the different components of the best-fit model. The exposure time is 400 ks. *Upper panel*: spectrum synthesized including the best-fit Gaussian component with a line width corresponding to a Doppler broadening of 1000 km s^{-1}. *Lower panel*: same as for the upper panel, but for a Doppler broadening of 2000 km s^{-1}.

While detection of the ^{44}Sc line is affected by absorption from the surrounding cold ejecta at early epochs (as predicted by Fransson & Chevalier 1987), we detect the ^{44}Sc line with high significance in spectra extracted from observations performed between 2016 and 2021, when the cold ejecta are expected to be optically thin. We measure a line flux $6.8^{+2.2}_{-2.3} \times 10^{-7}$ photons s^{-1} cm^{-2}, corresponding to an initial mass $M_{44} = (1.6 \pm 0.5) \times 10^{-4} M_\odot$. To our knowledge, this is the first firm detection of the Sc emission line in SN 1987A.

The precise estimation of the mass of ^{44}Ti depends on the actual size and morphology of the emitting region. As described in Sect. 3, our analysis was conducted assuming the ^{44}Sc emission as arising from a circular region of radius 0.3″. According to Larsson et al. (2023), we consider this extent an upper limit. As a result, our initial mass of ^{44}Ti must be considered as an upper limit value. Nevertheless, we show that even by assuming a different distribution of the line surface brightness, our results do not change significantly (<10%). Our estimate of the ^{44}Ti mass

is in close agreement with the *NuSTAR* analysis of (Boggs et al. 2015). However, it is significantly lower than that obtained by Grebenev et al. (2012) based on INTEGRAL observations.

Our value of M_{44} is also in good agreement with long-term 3D simulations of neutrino-driven explosions (Sieverding et al. 2023), assuming an explosion energy of $(1.3 - 1.5) \times 10^{51}$ erg (Arnett 1987; Utrobin 2005; Utrobin et al. 2021; Wang & Burrows 2024).

New *Chandra* observations will improve the statistics and provide a more constrained estimate of M_{44}.

In conclusion, our work provides an independent procedure for measuring the yield of ^{44}Ti in SN 1987A by analyzing soft X-ray emission. Future observations will further tighten these constraints.

Acknowledgements. M.M., V.S., E.G., S.O., and F.B. acknowledge financial contribution from the PRIN 2022 (20224MNC5A) – "Life, death and after-death of massive stars" funded by European Union – Next Generation EU, and the INAF Theory Grant "Supernova remnants as probes for the structure and mass-loss history of the progenitor systems". This paper is partially supported by the Fondazione ICSC, Spoke 3 Astrophysics and Cosmos Observations. National Recovery and Resilience Plan (Piano Nazionale di Ripresa e Resilienza, PNRR) Project ID CN_00000013 "Italian Research Center on High-Performance Computing, Big Data and Quantum Computing" funded by MUR Missione 4 Componente 2 Investimento 1.4: Potenziamento strutture di ricerca e creazione di "campioni nazionali di R&S (M4C2-19)" – Next Generation EU (NGEU). R.G., V.S., O.P. acknowledge partial support from the INAF mini-grant 1.05.23.04.04. This project was partially funded also through the MSCA4Ukraine project from the European Union. Views and opinions expressed are however those of the authors only and do not necessarily reflect those of the European Union. Neither the European Union nor the MSCA4Ukraine Consortium as a whole nor any individual member institutions of the MSCA4Ukraine Consortium can be held responsible for them. This work made use of the HPC system MEUSA, part of the Sistema Computazionale per l'Astrofisica Numerica (SCAN) of INAF-Osservatorio Astronomico di Palermo. S.N. is supported by JSPS Grant-in-Aid Scientific Research (KAKENHI) (A), Grant Number JP25H00675 and JST ASPIRE Program "RIKEN-Berkeley mathematical quantum science initiative. We acknowledge Andrea Damonte for his kind support on the MCMC chains.

References

Ahmad, I., Greene, J. P., Moore, E. F., et al. 2006, Phys. Rev. C, 74, 065803
Alp, D., Larsson, J., & Fransson, C. 2021, ApJ, 916, 76
Arnaud, K. A. 1996, in Astronomical Society of the Pacific Conference Series, 101, Astronomical Data Analysis Software and Systems V, eds. G. H. Jacoby, & J. Barnes, 17
Arnett, W. D. 1987, ApJ, 319, 136
Arnett, W. D., Bahcall, J. N., Kirshner, R. P., & Woosley, S. E. 1989, ARA&A, 27, 629
Basko, M. 1994, ApJ, 425, 264
Beuermann, K., Brandt, S., & Pietsch, W. 1994, A&A, 281, L45
Boggs, S. E., Harrison, F. A., Miyasaka, H., et al. 2015, Science, 348, 670
Borkowski, K. J., Reynolds, S. P., Green, D. A., et al. 2010, ApJ, 724, L161
Burrows, C. J., Krist, J., Hester, J. J., et al. 1995, ApJ, 452, 680
Cash, W. 1979, ApJ, 228, 939
Chevalier, R. A., & Dwarkadas, V. V. 1995, ApJ, 452, L45
Colgan, S. W. J., Haas, M. R., Erickson, E. F., Lord, S. D., & Hollenbach, D. J. 1994, ApJ, 427, 874
Cook, W. R., Palmer, D. M., Prince, T. A., et al. 1988, ApJ, 334, L87
Davis, J. E., Bautz, M. W., Dewey, D., et al. 2012, SPIE Conf. Ser., 8443, 84431A
Dotani, T., Hayashida, K., Inoue, H., et al. 1987, Nature, 330, 230
Frank, K. A., Zhekov, S. A., Park, S., et al. 2016, ApJ, 829, 40
Fransson, C., & Chevalier, R. A. 1987, ApJ, 322, L15
Grebenev, S. A., Lutovinov, A. A., Tsygankov, S. S., & Winkler, C. 2012, Nature, 490, 373
Greco, E., Miceli, M., Orlando, S., et al. 2021, ApJ, 908, L45
Greco, E., Miceli, M., Orlando, S., et al. 2022, ApJ, 931, 132
Haas, M. R., Colgan, S. W. J., Erickson, E. F., et al. 1990, ApJ, 360, 257
Haberl, F., Geppert, U., Aschenbach, B., & Hasinger, G. 2006, A&A, 460, 811
Hashimoto, M. 1995, Progr. Theor. Phys., 94, 663
Helder, E. A., Broos, P. S., Dewey, D., et al. 2013, ApJ, 764, 11
Jerkstrand, A., Fransson, C., & Kozma, C. 2011, A&A, 530, A45
Kaastra, J. S., & Bleeker, J. A. M. 2016, A&A, 587, A151
Kifonidis, K., Plewa, T., Janka, H. T., & Müller, E. 2003, A&A, 408, 621
Larsson, J., Fransson, C., Spyromilio, J., et al. 2016, ApJ, 833, 147
Larsson, J., Fransson, C., Sargent, B., et al. 2023, ApJ, 949, L27
Leising, M. D. 2006, ApJ, 651, 1019
Leising, M. D., & Share, G. H. 1990, ApJ, 357, 638
Lundqvist, P., & Fransson, C. 1991, ApJ, 380, 575
Luo, D., & McCray, R. 1991, in Bulletin of the American Astronomical Society, 23, 1406
Magkotsios, G., Timmes, F. X., Hungerford, A. L., et al. 2010, ApJS, 191, 66
Mahoney, W. A., Varnell, L. S., Jacobson, A. S., et al. 1988, ApJ, 334, L81
Maitra, C., Haberl, F., Sasaki, M., et al. 2022, A&A, 661, A30
Mao, J., Ono, M., Nagataki, S., et al. 2015, ApJ, 808, 164
Matz, S. M., Share, G. H., Leising, M. D., et al. 1988, Nature, 331, 416
Miceli, M. 2023, Plasma Phys. Controlled Fusion, 65, 034003
Miceli, M., Orlando, S., Burrows, D. N., et al. 2019, Nat. Astron., 3, 236
Nagataki, S. 2000, ApJS, 127, 141
Nagataki, S., Hashimoto, M.-a., Sato, K., & Yamada, S. 1997, ApJ, 486, 1026
Nagataki, S., Hashimoto, M.-a., Sato, K., Yamada, S., & Mochizuki, Y. S. 1998, ApJ, 492, L45
Ono, M., Nagataki, S., Ferrand, G., et al. 2020, ApJ, 888, 111
Orlando, S., Miceli, M., Pumo, M. L., & Bocchino, F. 2015, ApJ, 810, 168
Orlando, S., Miceli, M., Petruk, O., et al. 2019, A&A, 622, A73
Orlando, S., Ono, M., Nagataki, S., et al. 2020, A&A, 636, A22
Orlando, S., Miceli, M., Ono, M., et al. 2025, A&A, 699, A305
Panagia, N. 1999, in New Views of the Magellanic Clouds, 190, ed. Y. H. Chu, N. Suntzeff, J. Hesser, & D. Bohlender, 549
Park, S., Burrows, D. N., Garmire, G. P., Zhekov, S. A., & McCray, R. 2006, in The Tenth Marcel Grossmann Meeting. On recent developments in theoretical and experimental general relativity, gravitation and relativistic field theories, 1281
Ravi, A. P., Park, S., Zhekov, S. A., et al. 2021, ApJ, 922, 140
Ravi, A. P., Park, S., Zhekov, S. A., et al. 2024, ApJ, 966, 147
Sandie, W. G., Nakano, G. H., Chase, L. F., et al. 1988, in American Institute of Physics Conference Series, 170, Nuclear Spectroscopy of Astrophysical Sources, eds. N. Gehrels & G. H. Share (AIP), 66
Sapienza, V., Miceli, M., Bamba, A., et al. 2024a, ApJ, 961, L9
Sapienza, V., Miceli, M., Bamba, A., et al. 2024b, RNAAS, 8, 156
Sieverding, A., Kresse, D., & Janka, H.-T. 2023, ApJ, 957, L25
Sun, L., Vink, J., Chen, Y., et al. 2021, ApJ, 916, 41
Teegarden, B. J., Barthelmy, S. D., Gehrels, N., Tueller, J., & Leventhal, M. 1989, Nature, 339, 122
Thielemann, F.-K., Hashimoto, M.-A., & Nomoto, K. 1990, ApJ, 349, 222
Urushibata, T., Takahashi, K., Umeda, H., & Yoshida, T. 2018, MNRAS, 473, L101
Utrobin, V. P. 2005, Astron. Lett., 31, 806
Utrobin, V. P., Chugai, N. N., & Andronova, A. A. 1995, A&A, 295, 129
Utrobin, V. P., Wongwathanarat, A., Janka, H. T., et al. 2021, ApJ, 914, 4
Wang, T., & Burrows, A. 2024, ApJ, 974, 39
West, R. M. 1987, Mercury, 16, 80
Woosley, S. E., & Hoffman, R. D. 1991, ApJ, 368, L31
XRISM collaboration 2025, PASJ, in press

Appendix A: Observations

Table A.1 lists the *Chandra* observations analyzed in this paper. Horizontal lines marks the different groups that we selected for the spectral analysis (see Sect. 3 and Appendix B).

Table A.1. Observations.

Start Date	OBS ID	PI	RA	DEC	T_{exp} (ks)
2000-12-07	1967	McCray	05 35 28.00	-69 16 11.10	98.76
2001-12-12	2831	Burrows	05 35 28.00	-69 16 11.10	49.41
2002-05-15	2832	Burrows	05 35 28.00	-69 16 11.10	44.26
2002-12-31	3829	Burrows	05 35 28.00	-69 16 11.10	49.01
2003-07-08	3830	Burrows	05 35 28.00	-69 16 11.10	45.31
2004-01-02	4614	Burrows	05 35 28.00	-69 16 11.10	46.49
2004-07-22	4615	Burrows	05 35 28.00	-69 16 11.10	48.83
2004-08-26	4640	McCray	05 35 28.00	-69 16 11.10	56.83
2004-08-27	5362	McCray	05 35 28.00	-69 16 11.10	67.42
2004-08-30	4641	McCray	05 35 28.00	-69 16 11.10	72.48
2004-09-01	6099	McCray	05 35 28.00	-69 16 11.10	48.61
2004-09-05	5363	McCray	05 35 28.00	-69 16 11.10	43.45
2005-01-09	5579	Burrows	05 35 28.00	-69 16 11.10	31.87
2005-01-13	6178	Burrows	05 35 28.00	-69 16 11.10	16.48
2005-07-11	5580	Burrows	05 35 28.00	-69 16 11.10	23.75
2005-07-16	6345	Burrows	05 35 28.00	-69 16 11.10	20.99
2006-01-28	6668	Burrows	05 35 28.00	-69 16 11.10	42.34
2006-07-27	6669	Burrows	05 35 28.00	-69 16 11.10	36.45
2007-01-19	7636	Burrows	05 35 28.00	-69 16 11.10	33.51
2007-03-11	8523	Canizares	05 35 28.00	-69 16 11.00	29.65
2007-03-12	8537	Canizares	05 35 28.00	-69 16 11.00	12.73
2007-03-13	7588	Canizares	05 35 28.00	-69 16 11.00	27.21
2007-03-18	8538	Canizares	05 35 28.00	-69 16 11.00	20.69
2007-03-19	7589	Canizares	05 35 28.00	-69 16 11.00	25.27
2007-03-20	8539	Canizares	05 35 28.00	-69 16 11.00	24.78
2007-03-21	8542	Canizares	05 35 28.00	-69 16 11.00	17.85
2007-03-24	8487	Canizares	05 35 28.00	-69 16 11.00	28.67
2007-03-27	8543	Canizares	05 35 28.00	-69 16 11.00	30.66
2007-03-28	8544	Canizares	05 35 28.00	-69 16 11.00	19.12
2007-03-29	8488	Canizares	05 35 28.00	-69 16 11.00	31.66
2007-03-31	8545	Canizares	05 35 28.00	-69 16 11.00	20.46
2007-04-01	8546	Canizares	05 35 28.00	-69 16 11.00	30.64
2007-04-17	7590	Canizares	05 35 28.00	-69 16 11.00	35.55
2007-07-13	7637	Burrows	05 35 28.00	-69 16 11.10	25.72
2007-09-04	9581	McCray	05 35 28.00	-69 16 11.10	44.96
2007-09-05	9582	McCray	05 35 28.00	-69 16 11.10	44.17
2007-09-07	9580	McCray	05 35 28.00	-69 16 11.10	34.59
2007-09-09	7620	McCray	05 35 28.00	-69 16 11.10	34.62
2007-09-11	7621	McCray	05 35 28.00	-69 16 11.10	36.95
2007-09-12	9591	McCray	05 35 28.00	-69 16 11.10	12.85
2007-09-12	9592	McCray	05 35 28.00	-69 16 11.10	12.87
2007-09-14	9589	McCray	05 35 28.00	-69 16 11.10	39.53
2007-09-16	9590	McCray	05 35 28.00	-69 16 11.10	24.65
2008-07-01	9144	Burrows	05 35 28.00	-69 16 11.10	42.03
2008-07-04	9143	Burrows	05 35 28.00	-69 16 11.10	8.58
2009-01-05	10130	Burrows	05 35 28.00	-69 16 11.10	6.02
2009-01-12	10852	Burrows	05 35 28.00	-69 16 11.10	10.78
2009-01-13	10221	Burrows	05 35 28.00	-69 16 11.10	18.73
2009-01-15	10853	Burrows	05 35 28.00	-69 16 11.10	11.25
2009-01-17	10854	Burrows	05 35 28.00	-69 16 11.10	11.99
2009-01-18	10855	Burrows	05 35 28.00	-69 16 11.10	18.78
2009-07-06	10222	Burrows	05 35 28.00	-69 16 11.10	23.47
2009-09-08	10926	Burrows	05 35 28.00	-69 16 11.10	33.83
2010-03-17	12125	Burrows	05 35 28.00	-69 16 11.10	18.15
2010-03-17	12126	Burrows	05 35 28.00	-69 16 11.10	21.2
2010-03-28	11090	Burrows	05 35 28.00	-69 16 11.10	24.56

2010-09-28	13131	Burrows	05 35 28.00	-69 16 11.10	26.48
2010-09-29	11091	Burrows	05 35 28.00	-69 16 11.10	27.92
2011-03-01	12145	Canizares	05 35 28.00	-69 16 11.00	51.21
2011-03-04	13238	Canizares	05 35 28.00	-69 16 11.00	54.16
2011-03-06	13239	Canizares	05 35 28.00	-69 16 11.00	46.74
2011-03-13	12146	Canizares	05 35 28.00	-69 16 11.00	25.62
2011-03-25	12539	Burrows	05 35 28.00	-69 16 11.10	52.15
2011-09-21	12540	Burrows	05 35 28.00	-69 16 11.10	37.53
2011-09-22	14344	Burrows	05 35 28.00	-69 16 11.10	11.59
2012-03-28	13735	Burrows	05 35 28.00	-69 16 11.10	42.91
2012-04-01	14417	Burrows	05 35 28.00	-69 16 11.10	26.94
2013-03-21	14697	Burrows	05 35 28.00	-69 16 11.10	67.57
2013-09-28	14698	Burrows	05 35 28.00	-69 16 11.10	68.53
2014-03-19	15809	Burrows	05 35 28.00	-69 16 11.10	74.46
2014-09-17	17415	Burrows	05 35 28.00	-69 16 11.10	19.37
2014-09-20	15810	Burrows	05 35 28.00	-69 16 11.10	48.29
2015-09-17	16756	Burrows	05 35 28.00	-69 16 11.10	66.6
2016-09-19	17899	Burrows	05 35 28.00	-69 16 11.10	26.12
2016-09-23	19882	Burrows	05 35 28.00	-69 16 11.10	41.08
2017-09-21	20793	Burrows	05 35 28.00	-69 16 11.10	48.29
2017-09-23	19289	Burrows	05 35 28.00	-69 16 11.10	18.9
2018-03-14	20927	Park	05 35 28.00	-69 16 11.10	16.6
2018-03-15	21037	Park	05 35 28.00	-69 16 11.10	29.42
2018-03-18	21038	Park	05 35 28.00	-69 16 11.10	34.22
2018-03-19	20322	Park	05 35 28.00	-69 16 11.10	15.16
2018-03-23	21042	Park	05 35 28.00	-69 16 11.10	41.05
2018-03-25	21043	Park	05 35 28.00	-69 16 11.10	28.83
2018-03-26	21044	Park	05 35 28.00	-69 16 11.10	15.8
2018-03-27	20323	Park	05 35 28.00	-69 16 11.10	27.09
2018-03-28	21049	Park	05 35 28.00	-69 16 11.10	30.9
2018-03-29	21050	Park	05 35 28.00	-69 16 11.10	17.76
2018-03-30	21051	Park	05 35 28.00	-69 16 11.10	15.01
2018-03-31	21052	Park	05 35 28.00	-69 16 11.10	30.12
2018-04-02	21053	Park	05 35 28.00	-69 16 11.10	12.19
2018-09-15	20277	Burrows	05 35 28.00	-69 16 11.10	33.83
2018-09-16	21844	Burrows	05 35 28.00	-69 16 11.10	33.83
2019-09-17	21304	Burrows	05 35 28.00	-69 16 11.10	41.06
2019-09-18	22849	Burrows	05 35 28.00	-69 16 11.10	41.06
2020-09-12	22425	Burrows	05 35 28.00	-69 16 11.10	60.82
2020-09-17	24652	Burrows	05 35 28.00	-69 16 11.10	29.33
2021-10-25	23534	Burrows	05 35 28.00	-69 16 11.10	29.00
2021-10-27	24295	Burrows	05 35 28.00	-69 16 11.10	30.00
2021-10-28	24654	Burrows	05 35 28.00	-69 16 11.10	30.00

Appendix B: Flux temporal evolution

Motivated by the detection of the ^{44}Sc emission line in the 2016-2021 spectra, we repeated the spectral analysis described in Sect. 3 on earlier epochs, dividing the data into three additional groups, namely Group 1 for observations performed between 2000 and 2004, Group 2 for those in 2005 − 2009, and Group 3 for 2010 − 2015. Figure B.1 shows the spectra of the different Groups. We measure the flux of the emission line centered at 4.076 keV in all the Groups, the line flux (corrected for the PSF effects) being $F_1 = 1.4^{+0.2}_{-0.3} \times 10^{-7}$ photons s^{-1} cm^{-2}, $F_2 < 3.9 \times 10^{-8}$ photons s^{-1} cm^{-2}, $F_3 = 7.3^{+2.2}_{-5.2} \times 10^{-8}$ photons s^{-1} cm^{-2} in Group 1, Group 2, and Group 3, respectively (error bars at 90% confidence level). As expected, the line flux in Groups 1 − 3, is significantly lower than that in Group 4. This is likely the result of the cold ejecta being still optically thick at these epochs. However, discussing the time evolution of the line flux is beyond the scope of this paper, given its intrinsic complexity related to (i) the complex effect of the absorption of cold ejecta, which monotonically (but non-linearly) decreases with time, (ii) the expansion of the bright X-ray ring (which decreases the fraction of photons spilling from the ring into our extraction region); and (iii) the increase of the hard X-ray flux (3 − 8 keV; see Ravi et al. 2024), which increases the contamination from the ring.

We also checked that the line is not significantly detected in the spectra of the ring (as already shown by Leising 2006 for the first *Chandra* observations). As an example, we explored the spectra in 2014 and 2020 finding that the line flux is always compatible with 0 at the 68% confidence level. Figure B.2 shows that the line emission is always well below the continuum.

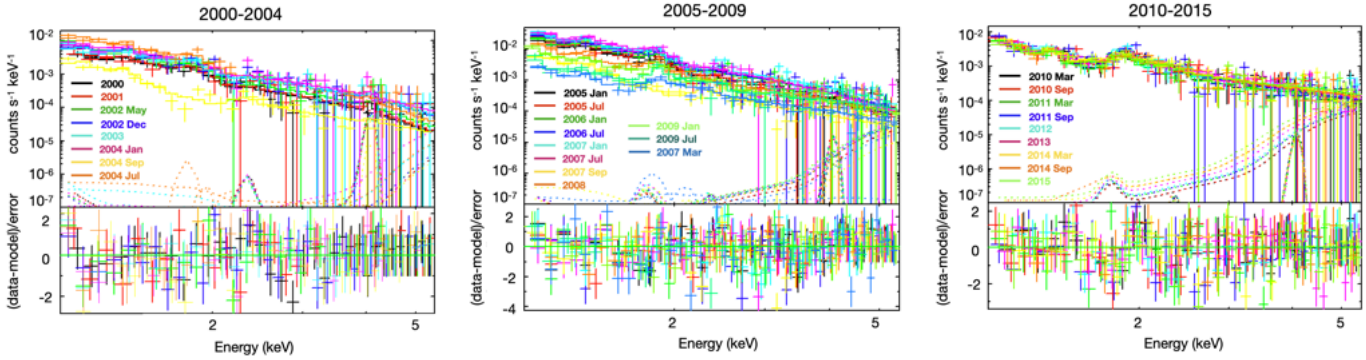

Fig. B.1. *Chandra*/ACIS spectra extracted from the circular region shown in Fig. 1 for all observations performed between 2000 and 2004 (*left*), 2005-2009 (*center*), and 2010-2015 (*right*) with the corresponding best-fit model and residuals.

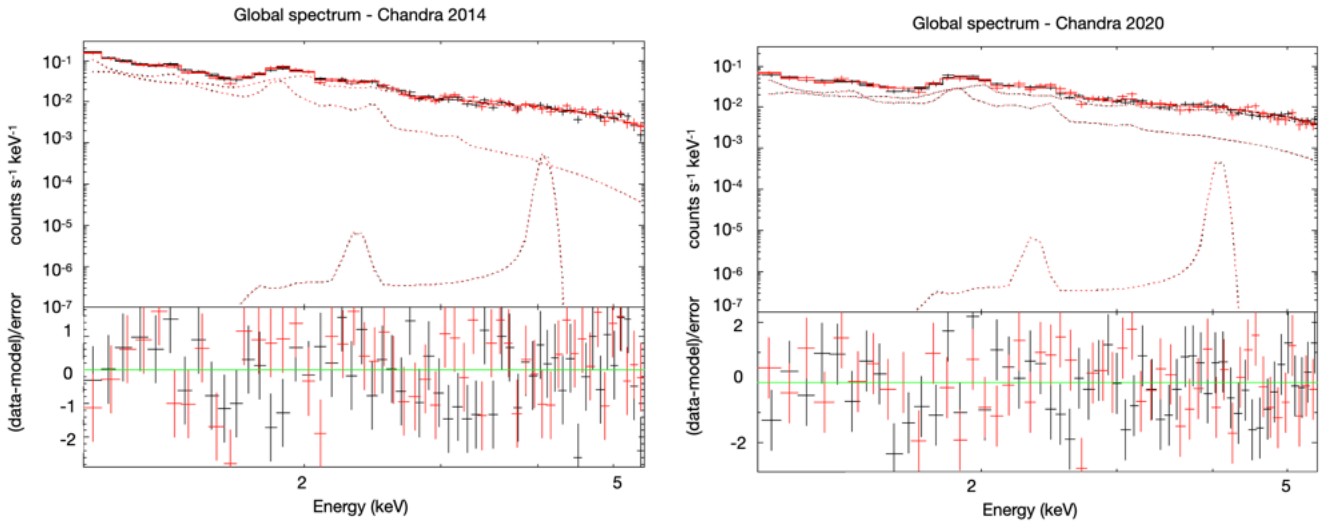

Fig. B.2. Spectra of the X-ray emission originating from a region including the ER of SN1987A at two different epochs – 2014 (*left panel*) and 2020 (*right panel*) – with the corresponding best fit model and residuals.

Appendix C: Background spectrum

Figure C.1 shows our choice of the background extraction region together with an example of the background spectrum, fitted with the following model:

$$Bkg\ model = const * (pow + apec + gauss + gauss + gauss). \quad \text{(C.1)}$$

In all of the background spectra the best fit model includes a power law taking into account the continuum, the model `apec` fitting the emission spectrum from collisionally ionized diffuse gas , based on the database AtomDB version 3.09 https://heasarc.gsfc.nasa.gov/xanadu/xspec/manual/XSmodelApec.html, plus three emission lines centered at energies which are less than 3 keV.

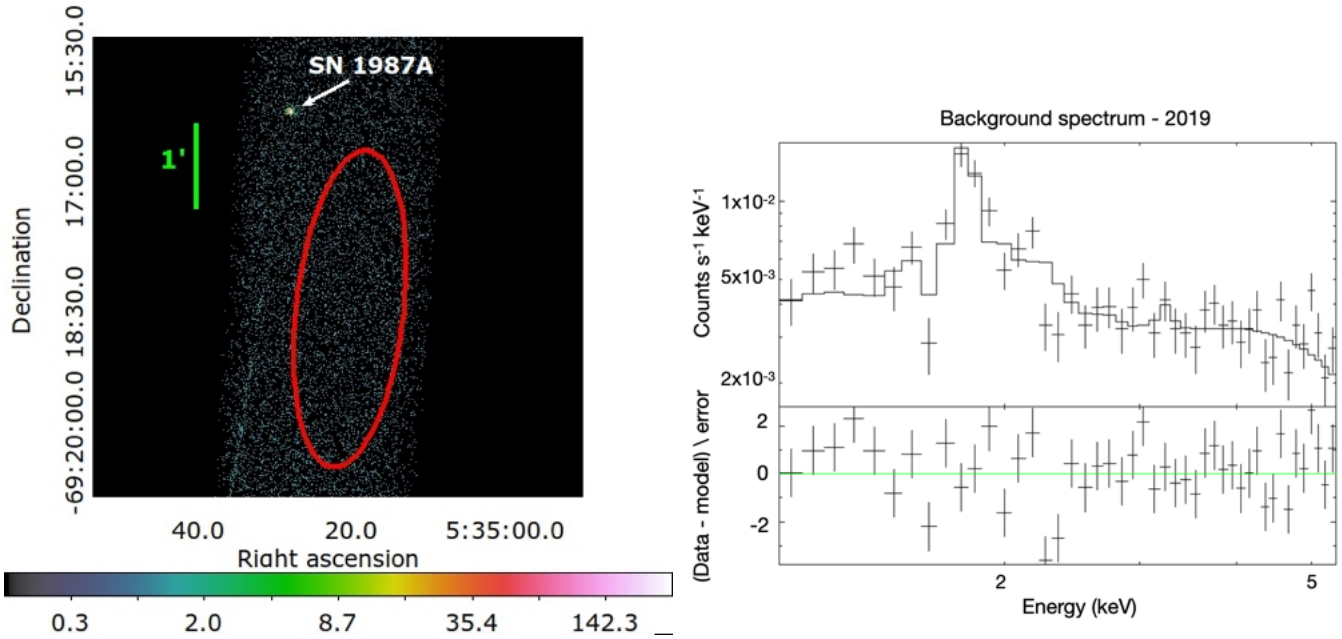

Fig. C.1. *Left panel*: *Chandra*/ACIS count map for Obs ID 21304 (same as in Fig. 1) in log scale. The red ellipse shows the background extraction region. *Right panel:* Spectrum extracted from the background region in the left panel with the corresponding best fit model (Eq. (C.1)) and residuals.

Appendix D: Corner plot

Figure D.1 presents the MCMC corner plot for the simultaneous analysis of the spectra collected between 2016 and 2021. Each panel shows the correlation between two different free parameters, indicated as `parameter_number`. In this case, `norm_24` is the flux associated with the ^{44}Sc emission line. All the temperature, ionization times and normalization are associated with the `vnei` component fitted for each spectrum.

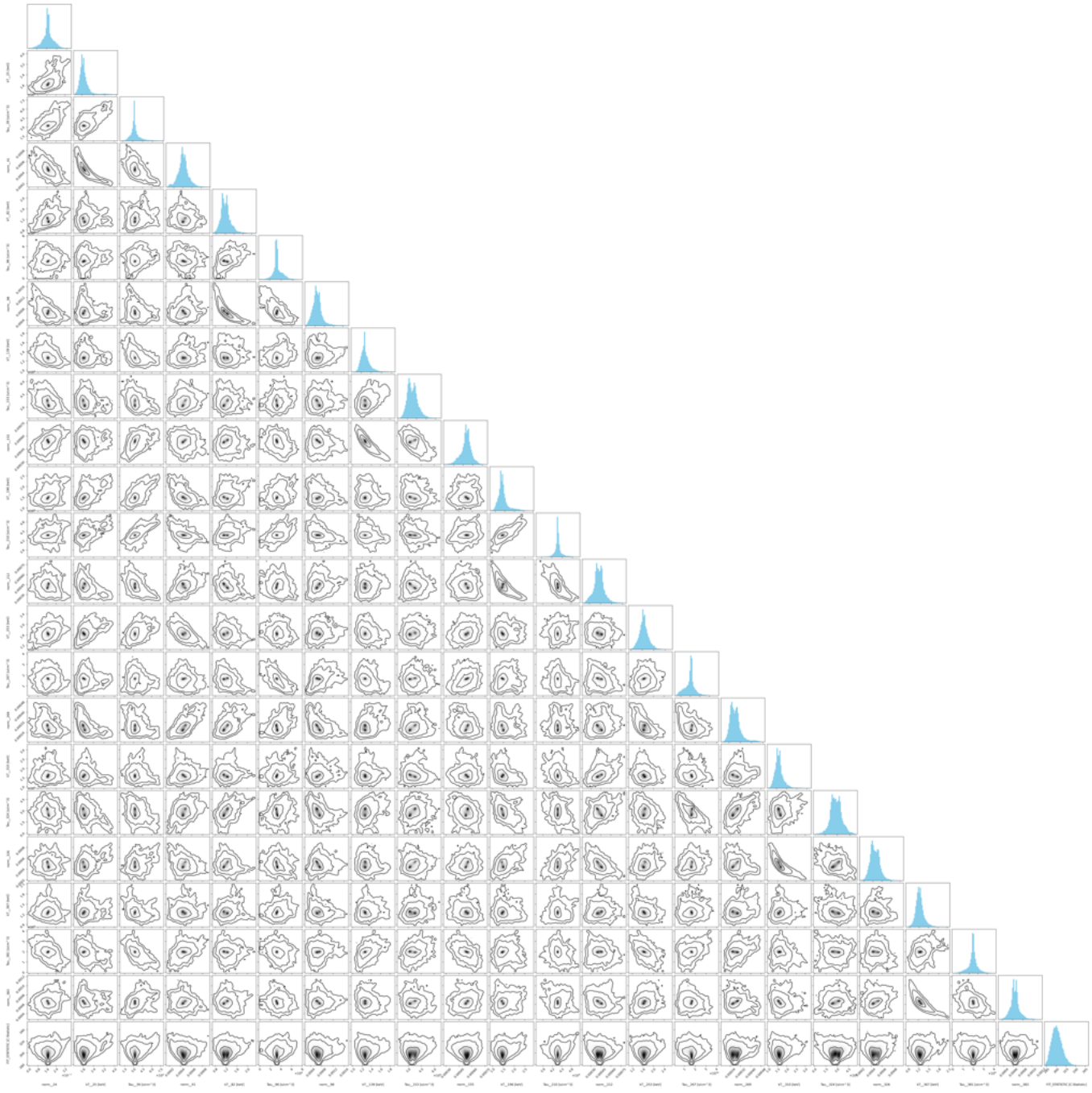

Fig. D.1. MCMC Corner plot for the simultaneous fit of 2016-2021 spectra (see Sects. 2 and 3).